

1
2
3
4
5
6
7
8
9
10
11
12
13
14
15
16
17
18
19
20
21
22
23

Towards a More Objective and High-throughput Spheroid Invasion Assay Quantification Method

Rozanne W. Mungai¹, Roger J. Hartman II², Grace E. Jolin¹, Kevin W. Piskorowski¹ and Kristen L. Billiar^{1*}

¹Department of Biomedical Engineering, Worcester Polytechnic Institute, Worcester, MA, USA 01605

²No affiliations, independent researcher

*Correspondence to:
Kristen L. Billiar
Biomedical Engineering Department
Worcester Polytechnic Institute
100 Institute Road
Worcester, MA 01609
kbilliar@wpi.edu
Phone: +1 (508) 8315000 x5384

1 **ABSTRACT**

2 Multicellular spheroids embedded in 3D hydrogels are prominent *in vitro* models for 3D cell
3 invasion. Yet, quantification methods for spheroid cell invasion that are high-throughput, objective and
4 accessible are still lacking. Variations in spheroid sizes and the shapes of the cells within render it
5 difficult to objectively assess invasion extent. The goal of this work is to develop a high-throughput
6 quantification method of cell invasion into 3D matrices that minimizes sensitivity to initial spheroid size
7 and cell spreading and provides precise integrative directionally-dependent metrics of invasion. By
8 analyzing images of fluorescent cell nuclei, invasion metrics are automatically calculated at the pixel
9 level. The initial spheroid boundary is segmented and automated calculations of the nuclear pixel
10 distances from the initial boundary are used to compute common invasion metrics (i.e., the change in
11 invasion area, mean distance) for the same spheroid at a later timepoint. We also introduce the area
12 moment of inertia as an integrative metric of cell invasion that considers the invasion area as well as the
13 pixel distances from the initial spheroid boundary. Further, we show that principal component analysis
14 can be used to quantify the directional influence of a stimuli to invasion (e.g., due to a chemotactic
15 gradient or contact guidance). To demonstrate the power of the analysis for cell types with different
16 invasive potentials and the utility of this method for a variety of biological applications, the method is
17 used to analyze the invasiveness of five different cell types. In all, implementation of this high-throughput
18 quantification method results in consistent and objective analysis of 3D multicellular spheroid invasion.
19 We provide the analysis code in both MATLAB and Python languages as well as a GUI for ease of use
20 for researchers with a range of computer programming skills and for applications in a variety of biological
21 research areas such as wound healing and cancer metastasis.

22

23

24

25

1 INTRODUCTION

2 Cell invasion and migration are driving factors for various biological events such as development
3 [1,2], wound healing [3-6], tumor metastasis [7-9] and host cell infiltration of implanted scaffolds [10-
4 13]. The effects of soluble and immobilized chemical gradients on cell migration on 2D surfaces and
5 infiltration into 3D matrices and tissues is well established [9,14]; however, it is also becoming clear that
6 mechanical cues play a large role in cell invasion and migration [7,15]. Cells move in response to
7 physical cues such as stiffness gradients [9,15,16], contact guidance [9,15,17,18] and mechanical restraint
8 [15,19-29].

9 *In vitro* models consisting of multicellular spheroids embedded in ECM are commonly used for
10 investigating the mechanisms of cell invasion into extracellular matrices (ECM) in a variety of diseases
11 [30-36]. Low contrast phase imaging is often used to capture images of cell invasion as it accommodates
12 live-imaging. However, phase images of spheroid invasion are difficult to analyze with common
13 automated software. Thus, this method often requires manual tracing of cell boundaries in programs such
14 as ImageJ/FIJI to quantify the extent of invasion via measuring the distances and areas of migrating cells
15 [8,30,37-43]. This manual tracing is time consuming and introduces subjectivity and possible technical
16 error. Alternatively, high-contrast fluorescent images are amenable to automated quantification using
17 common analysis software which allows for more objective high-throughput analysis. However,
18 fluorescent images are less accommodating for live imaging as they require transfection of fluorescent
19 proteins [44] or adding live cell stains which do not give a strong signal-to-noise ratio [45]. To overcome
20 this limitation, clear high contrast fluorescence images can be captured by fixing and staining samples at
21 the experiment endpoint using common accessible dyes. After imaging, the cell invasion can be
22 quantified (such as with migration tracks [8,46]) using image analysis software or custom programs, and
23 invasion metrics can be calculated.

1 Quantification metrics for cell invasion into 3D matrices commonly involve the overall invasion area
2 and/or the distance travelled by cells at a given timepoint [30,34,37,38,41,43,44,47-49]. The invasion area
3 is used to represent the number of invaded cells [30,34,37,38,41,43,44,49-51], and the distance travelled
4 is often reported as either the mean or maximum distance travelled by cells [8,30,41,49,52]. Yet, these
5 metrics are sensitive to changes in cell size and shape that occur as cells migrate through the matrix
6 [53,54]. In the case of multicellular spheroid *in vitro* models, when invasion area and distance travelled
7 are calculated without taking into account the initial spheroid boundary, these metrics are also sensitive to
8 differences in size and shape of the spheroids. A metric that takes into account both the invasion area and
9 distance travelled is especially useful, such as the migration index published by Liu *et al.* [30], as it
10 informs both how many and how far cells are invading. The types of quantification metrics that can be
11 calculated are limited by the methods used to capture and quantify images, especially if a common or
12 microscope-based software is used. Therefore, there is a need for an easy-to-implement method and
13 corresponding computational analysis tool that is precise and objective, offers flexibility in quantification,
14 and is simple to use for a researcher unfamiliar with programming.

15 Here we present a high-throughput automated quantification method of cell invasion into 3D
16 matrices using a complementary pixel-based method to segmentation methods. Multicellular spheroids
17 embedded in collagen hydrogels are live-stained for cell nuclei, which are easy to image and are more
18 resistant to shape changes during invasion than the cell body, and the distribution of nuclear pixels is
19 quantified. Live fluorescent imaging allows for precise segmentation of the initial spheroid boundary,
20 thus minimizing the effects of spheroid initial size and shape. Automated calculations of the invasion area
21 as well as distances and angles of nuclear pixels from the boundary are calculated—metrics that are
22 relatively insensitive to initial spheroid size. We introduce the area moment of inertia, which takes into
23 account both the area and distances of nuclear pixels of invading cells, as an integrative metric for the
24 overall extent of invasion. In combination with principal component analysis, the area moment of inertia
25 metric is also used to quantify invasion directionality in response to anisotropic mechanical constraint.

1 Five different cell types are included to demonstrate the applicability of the analysis for cell types with
2 different invasive potentials, and we provide an open-source graphical interface and the detailed code in
3 both MATLAB and Python languages for ease of adoption by researchers with a range of computer
4 programming skills.

5

6 **MATERIALS AND METHODS**

7 *Ethics*

8 No experiments were performed on humans or animals for this study; therefore, ethics approval is not
9 required. Freshly isolated cells used in this study were harvested from animal (pig) tissue while all other
10 cells, including human cells, were obtained as a gift.

11

12 *Cell types and culture conditions*

13 Cell spheroids of various cell types were embedded in collagen hydrogels and allowed to invade the
14 matrix for two days. The cell types were chosen to span mesenchymal and epithelial cell type
15 classifications as they are known to be motile and immotile respectively. Valvular interstitial cells (VIC),
16 dermal fibroblasts and smooth muscle cells (SMC) are the mesenchymal cell types studied to highlight
17 differences in invasive potential within the group and were compared to epithelial RPE-1 cells. PC9 cells
18 were also included as we are interested in how a cancerous epithelial cell type (having undergone the
19 endothelial-to-mesenchymal transformation) compares to non-cancerous mesenchymal cell types.

20 Porcine aortic VICs were isolated from fresh pig hearts obtained from a local abattoir (Blood
21 Farm, Groton, MA), and the VICs were isolated within three hours as per published protocols [20] and
22 used in experiments between passages 2-8. Neonatal human dermal fibroblasts (NHF), originally
23 harvested from de-identified donated male foreskin tissue, were obtained as a gift from Dr. George Pins
24 (Worcester Polytechnic Institute) and used in experiments between passages 6-12. Immortalized WKY

1 3M-22 male rat aortic SMCs were obtained as a gift from Dr. Marsha Rolle (Worcester Polytechnic
2 Institute). The immortalized female human retinal pigment epithelial cell line (RPE-1) was obtained as a
3 gift from Dr. Amity Manning (Worcester Polytechnic Institute). The same culture medium base
4 formulation and conditions were used for all of the above cell types: DMEM (Gibco) supplemented with
5 10% v/v fetal bovine serum and 1% v/v antibiotic-antimycotic (Gibco). For the SMCs, 1% v/v MEM non-
6 essential amino acids (Gibco) were added to maintain a growth phenotype. The PC9 human lung
7 adenocarcinoma cell line was also obtained as a gift from Dr. Amity Manning and were cultured in
8 RPMI-1640 (GenClone, Genessee Scientific) supplemented with 10% v/v fetal bovine serum and 1% v/v
9 antibiotic-antimycotic (Gibco). The identity of the PC9 cancer cells have been previously confirmed by
10 STR analysis [55]. The cell cultures were maintained at 37°C in a humidified 5% CO₂-containing
11 incubator.

12

13 *Generation of multicellular spheroids*

14 3D spheroids were generated for each cell type as in our previous work [56]. Briefly, the cells were
15 trypsinized, resuspended, and stained with 5µg/mL Hoechst 33342 (Invitrogen) for 10 minutes at 37°C for
16 visualization of cell nuclei. The stain was then diluted, and the cells were resuspended at a cell
17 concentration of one million cells per 200 µL. Non-adherent agarose microwells were generated by
18 pipetting a pre-warmed 2% w/v agarose solution (MilliporeSigma), made in DMEM, into negative molds
19 with 500 µm diameter wells (24-96 or 12-256; Microtissues®), and the agarose was allowed to solidify.
20 The stained cell suspension was seeded into the prepared agarose microwells, and the cells were allowed
21 to settle into spheroids for one day (Supplementary Fig. 1) before embedding them into collagen
22 hydrogels.

23

24 *Embedding of multicellular spheroids into collagen gels*

1 The multicellular spheroids were harvested from the microwells and suspended in media. Cooled rat tail
2 collagen type I (Advanced Biomatrix, RatCol®) was then mixed with neutralization solution following
3 manufacturer's recommendations to make collagen hydrogels. The spheroid suspension was mixed into
4 the collagen solution for ~ 20 spheroids/mL in a final collagen concentration of 2 mg/mL. Next, the
5 solution was poured into well plates and allowed to gel for 30 minutes at 37°C. The well plates used were
6 either a tissue culture plastic 6-well plate for maximizing gel volume, or a flexible silicone well plate with
7 small side posts (CellScale MechanoCulture FX™) to restrict gel compaction (4x4 array of 8 mm x 8 mm
8 square wells).

9 Fresh medium was added over the samples, and the samples were imaged (Day 0) as described
10 below. After imaging, the samples were returned to 37°C in a humidified 10% CO₂-containing incubator
11 and allowed to culture for two days (Supplementary Fig. 2). The timepoint of two days was chosen to
12 allow sufficient time for cells to invade into the matrix while minimizing migration past the camera field
13 of view.

14 15 *Staining and Imaging*

16 The extent of cell invasion and migration was assessed by capturing images of the cell nuclei as 10µm-
17 spaced z-stack slices through the thickness of the spheroids using a Keyence BZ-X810 fluorescence
18 microscope (6.1µm DOF, High Resolution setting: 6dB gain, Binning off). The z-slices demonstrated
19 consistent staining intensity through the depth of the spheroids (Supplementary Fig. 3). On Day 0, the
20 spheroids, pre-stained with Hoechst during spheroid formation, were imaged live immediately after
21 gelation of the collagen, and the spheroid locations were saved for use again during Day 2 imaging. On
22 Day 2, the samples were fixed with 4% paraformaldehyde, permeabilized using 0.25% Triton-X 100 and
23 stained again with Hoechst, at a 1:1000 dilution to obtain a strong fluorescent signal in the nuclei. They
24 were further stained for F-actin visualization using Alexa Fluor® 488 phalloidin (Life Technologies) at a
25 1:100 dilution. The images of each z-stack were processed using the Keyence BZ-X800 Analyzer to

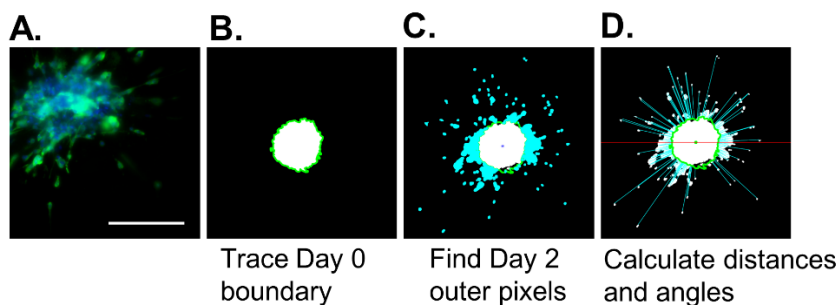
1 create maximum z-projection images (Fig. 1A, Supplementary Fig. 4), increase the image contrast and
2 convert them to grayscale.

3 Because the spheroids are mixed into the collagen hydrogel solution, it was common to observe
4 spheroids that were close to each other or out of the vertical field-of-view. Spheroids that were out of the
5 field of view or too close together (less than 400 μm apart or with migration paths of different spheroids
6 that could cross) were not imaged (Supplementary Fig. 5).

7
8 *Quantification of cell invasion and migration into matrix*

9 Image quantification was carried out using a custom MATLAB program (MathWorks®) using the image
10 processing package. The grayscale images were contrast enhanced, background subtracted if needed, and
11 binarized with a global threshold strategy. A circular mask was then applied to the images to prevent
12 biases towards the long axis and corners of the frame by excluding those pixels. For each set of Day 0 and
13 Day 2 binarized images, the Day 0 spheroid edge was located and automatically segmented to determine
14 the boundary of cell invasion (Fig. 1B). The centroids of the Day 0 and Day 2 spheroids were identified
15 and used to overlap the Day 0 boundary and the Day 2 binarized image. From there, the locations of all
16 the pixels of the Day 2 image that lay outside of the boundary were found (i.e., “the outer pixels”) (Fig.
17 1C), and the distances of each of these pixels from both the boundary and the spheroid centroid were
18 calculated as well as their angles from the centroid, measured clockwise from the x-axis (as in a polar
19 coordinate system) (Fig. 1D).

20



21

1 **Figure 1:** Z-stack image processing and quantification. Images were processed to create maximum z-
2 projection images from each z-stack as demonstrated by a representative Day 2 image (A). The Day 0
3 boundary was segmented (B) and the pixels of the Day 2 image located past the boundary were identified
4 (C). The distances and angles of pixels outside of the boundary were calculated with reference to the
5 spheroid boundary and center. For clarity, only a portion of the distance lines are shown (D). Scale bar:
6 200 μm . Panel A: Representative spheroid is imaged at 20X magnification and off-set to highlight
7 invading cells. Panels B-D: 10X magnification.

8

9 The change in spheroid area (ΔA) i.e., the stained pixel area outside of the initial spheroid boundary, is
10 calculated by summing the number of pixels in the image and subtracting the Day 2 area to the Day 0
11 area, equation (1).

$$\Delta A = Area_{Day\ 2} - Area_{Day\ 0} \quad (1)$$

15 By locating the individual pixels in the images, rather than cell or nuclei centroids, pixel-level distance
16 calculations can be performed which avoids the difficulty of distinguishing clustered cells. The distance
17 (d) is calculated from the differences of the x and y distances from the boundary (x_b, y_b) and the outer
18 pixels (x_p, y_p) along a radial line emanating from the centroid of the Day 0 image to the outer pixel,
19 equation (2) (Fig. 1D):

$$d = \sqrt{(x_p - x_b)^2 + (y_p - y_b)^2} \quad (2)$$

22 The angles of invasion are obtained by calculating the arctangent of the x and y distances to the spheroid
23 centroid, (x_0, y_0), equation (3).

$$\theta = \tan^{-1} \frac{y_p - y_0}{x_p - x_0} \quad (3)$$

26

1 The invasion area moment of inertia (I) was evaluated as an integrative measure of the area change and
2 the distance from the spheroid boundary. The radial moment, I_r , was calculated by summing over the
3 squared radial distances (r) of each outer pixel (i) to the boundary, where dA is the area of each pixel,
4 equation (5).

$$I_r = \sum_{i=0}^n r^2 dA$$

(5)

7 *Principal component analysis*

8 In addition to being able to quantify the directional migration along the camera x- and y-axes, the
9 invasion area moment of inertia can be calculated along any arbitrary axes (x' , y') using coordinate
10 transformation. Most notably, the directions of maximum and minimum invasion and extent of invasion
11 in each direction can be expediently calculated using principal component analysis (PCA). Coordinate
12 transformations were performed in MATLAB to reorient the distance values along the principal
13 components (directions of maximum and minimum invasion). The extent of invasion is then determined
14 by calculating the directional moments of inertia ($I_{x'}$ and $I_{y'}$) along the principal axes, by summing the
15 transformed directional distances, equation (6), and calculating the mean distance in the principal
16 directions.

$$I_{x'} = \sum_{i=0}^n y'^2 dA ; I_{y'} = \sum_{i=0}^n x'^2 dA$$

(6)

21 *Code availability*

22 Our custom MATLAB image analysis program is shared on GitHub to facilitate use by other researchers.

23 <<https://github.com/rmungai/SpheroidInvasionAnalysis>>

1 To expand user accessibility, we have published a Python version of the program as well as a
2 downloadable GUI for users without computer programming backgrounds.
3 <<https://github.com/rogerh2/SpheroidInvasionAnalysis>>

4 Detailed descriptions of the scripts are also included on the GitHub pages.

5

6

7 *Statistical analysis*

8 An outlier analysis was performed on the dataset using MATLAB by detecting and removing values more
9 than three scaled median absolute deviations (MAD) from the median. The normality of the data set was
10 assessed using MATLAB via the D'Agostino & Pearson omnibus normality test employing a significance
11 level $\alpha=0.05$. After determination of normality, significant differences among groups were analyzed
12 using the sjstats library in R using one-way analysis of variance (ANOVA) followed by Tukey's Honest
13 Significant Difference (HSD) post hoc test. Violin plots of the area change, mean distance from the
14 boundary, and area moment of inertia per spheroid were generated using the ggplot library in R and were
15 utilized to show the entire data distribution of all spheroids. Numbers of spheroids and biological
16 replicates are provided in the figure captions.

17

18 **RESULTS**

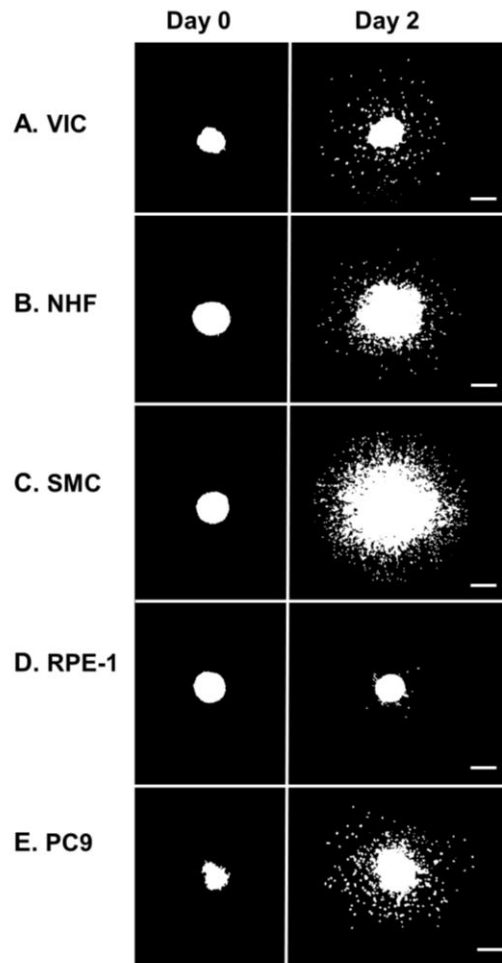
19 *Image quantification of spheroid invasion*

20 Images of the embedded spheroids demonstrate that all cell types invaded into the collagen hydrogel with
21 the extent of invasion varying substantially among cell types (Fig. 2, Supplementary Fig. 4).

22 Qualitatively, the RPE-1 cells demonstrated the least invasion while the SMCs demonstrated the most

1 invasion. The PC9 cells demonstrated the second-most invasion with the NHFs and VICs following,
2 respectively.

3



4

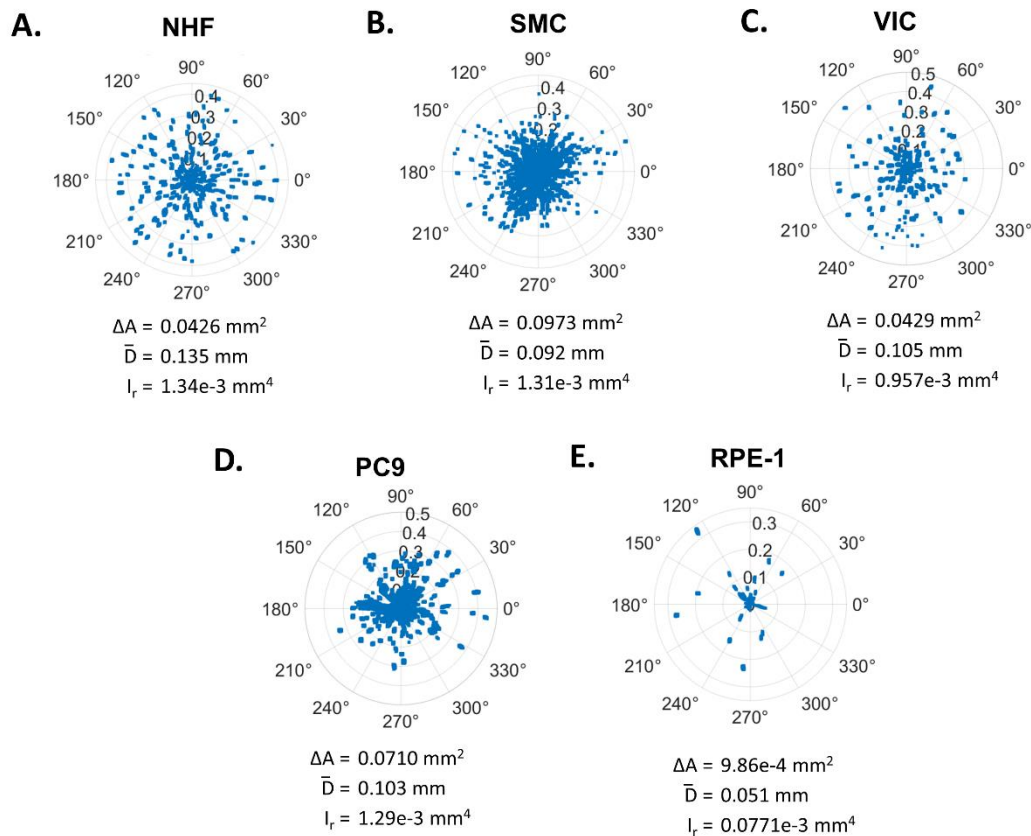
5

6 **Figure 2:** Invasion of cells from spheroids into collagen hydrogels. Representative images of invasion on
7 Day 0 compared to Day 2, VIC (A), NHF (B), SMC (C), RPE-1 (D) and PC9 (E). Binarized maximum
8 projection images of cell nuclei stained with Hoechst fluorescent dye at 10X magnification. Scale bar:
9 200 μm .

10

11 The binarized images were analyzed using our custom MATLAB program to obtain polar plots depicting
12 spheroid invasion past the boundary and calculate quantitative metrics for each cell type to demonstrate
13 the nuances of each invasion metric (Fig. 3). The area change is not necessarily correlated with distance

1 as demonstrated by comparing representative NHF and SMC polar plots (Fig. 3A&B). The SMCs do not
2 invade as far as the NHFs, resulting in a lower distance, but they do have a higher area change which
3 results in an area moment of inertia with a nearly equal value ($\sim 0.001 \text{ mm}^4$) for both cell types since the
4 moment incorporates both the distance of invasion and area change.



5

6 **Figure 3:** Visualization of variation of invasion behavior across cell types. Polar plots demonstrate
7 invasion behavior of individual spheroids at Day 2. The distance (μm) versus angle is plotted for each
8 pixel past the Day 0 spheroid boundary for VIC (A), NHF (B), SMC (C), RPE-1 (D) and PC9 (E). The
9 boundary is represented as the plot center (0,0). Invasion metrics for representative spheroids, area
10 change, ΔA , mean distance, \bar{D} , radial moment, I_r , as defined in the text, are provided below each plot.

11

12 *Directional invasion assessment*

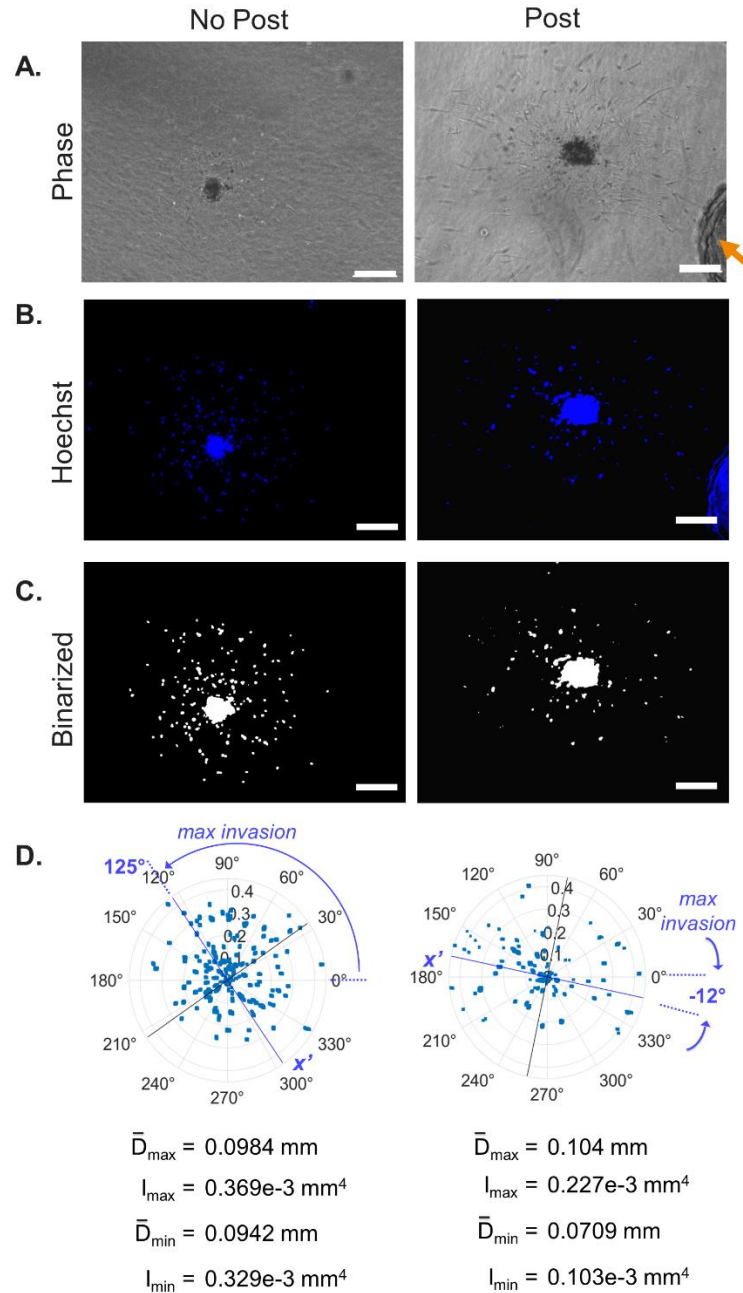
13 We aimed to demonstrate that the area moment of inertia can be used to assess invasion directionality

14 resulting from a guidance cue, particularly in cases where directional invasion does not exclusively occur

1 along the x- and y- axes. We performed principal coordinate analysis (PCA) to a representative spheroid
2 exhibiting directional invasion due to its proximity to a stiff silicone post within the gel (Fig. 4A, right).
3 The post introduces constraint in the hydrogel which causes directional invasion towards it via contact
4 guidance [46,57-59]. A binarized image of the spheroid demonstrating directional invasion was corrected
5 to mask the post from the image (Fig. 4C, right) and quantified as described above. PCA resulted in the
6 determination of the principal angles of maximum and minimum cell invasion (Fig. 4D, right). A
7 coordinate transformation was then performed to calculate the extent of invasion along the principal
8 angles via the mean distance (0.104 mm and 0.071 mm) and the directional area moments of inertia
9 ($0.227e-3 \text{ mm}^4$ and $0.103e-3 \text{ mm}^4$). The fold change of mean distances and directional moments were
10 calculated (by taking the ratio of the maximum to minimum directions) and found to be 1.5X and 2.2X
11 greater in the direction of the post, respectively, thus indicating directional invasion. To validate the
12 directional analysis method, a control spheroid (which was not located next to a post) was also quantified
13 for comparison (Fig 4, left). The mean distances along the principal angles for the control spheroid were
14 found to be 0.0984 and 0.0942 mm, and the directional moments were found to be $0.369e-3 \text{ mm}^4$ and
15 $0.329e-3 \text{ mm}^4$ (Fig 4D, left) resulting in fold change values of 1.1X for both metrics. In comparison, the
16 mean distances and directional moments fold change values are 1.4X and 2X greater for the spheroid with
17 the post (Fig 4, right). Taken together, these results demonstrate that this method effectively detects and
18 quantifies invasion directionality.

19

20



1

2

3 **Figure 4:** Quantification program also assesses invasion directionality. Directional invasion was
 4 demonstrated by imaging a collagen gel-embedded VIC spheroid growing near a structural post (indicated
 5 by arrow) of the culture well for four days. Phase, Hoechst-stained and binarized spheroid images on Day
 6 2 (no post control) and Day 4 (spheroid with post). Scale bar: 200 μm (A-C). PCA of quantified data
 7 plotted as a polar plot centered at the mean. Principal angles are indicated (blue line: maximum invasion
 8 at 125° and -12°; black line: minimum invasion). Polar plot depicts the distance from the boundary (mm)
 9 versus angle for each pixel. Mean distances and directional moments along the principal angles were
 10 calculated to quantify invasion directionality and are provided below the polar plot (D).

11

1 *Statistical comparison of invasion between groups*

2 Comparing the five cell types together, the change in area from Day 2 compared to Day 0 was found to be
3 the highest for the SMCs and all other cell types had a significantly reduced area change in comparison
4 indicating SMCs as the most invasive (Fig. 5A). The PC9 cells had the second-highest area change
5 followed by the NHF, VIC, and RPE-1 cells respectively. The area change of the PC9 cells was
6 significantly higher than that of the RPE-1 demonstrating that, as expected, the cancerous epithelial cell
7 type is much more invasive than the wild-type epithelial cell type.

8 For the mean invasion distance, SMCs and NHFs were found to have the longest distance
9 followed by VIC, PC9 and RPE-1 cells (Fig. 5B). All cells had a significantly higher mean distance than
10 the RPE-1 cells, demonstrating that the epithelial cell type was, as expected, the least motile compared to
11 the more migratory mesenchymal-type and cancer cells. SMCs did not demonstrate a significantly longer
12 distance than other cells apart from RPE-1. This difference in the SMC results for area change and
13 distance demonstrates that a high invasion area change does not necessarily indicate a longer invasion
14 distance.

15 For the radial area moment of inertia of invasion (I_r), the SMCs were found to have the highest
16 value which was significantly higher than all the other cell types, as with area change (Fig. 5C). Since the
17 area moment of inertia metric incorporates both invasion area and distance into the calculation, the
18 moment calculation demonstrates that SMCs are the most invasive cell type overall, a finding that may
19 have been overlooked if invasion distance was used alone.

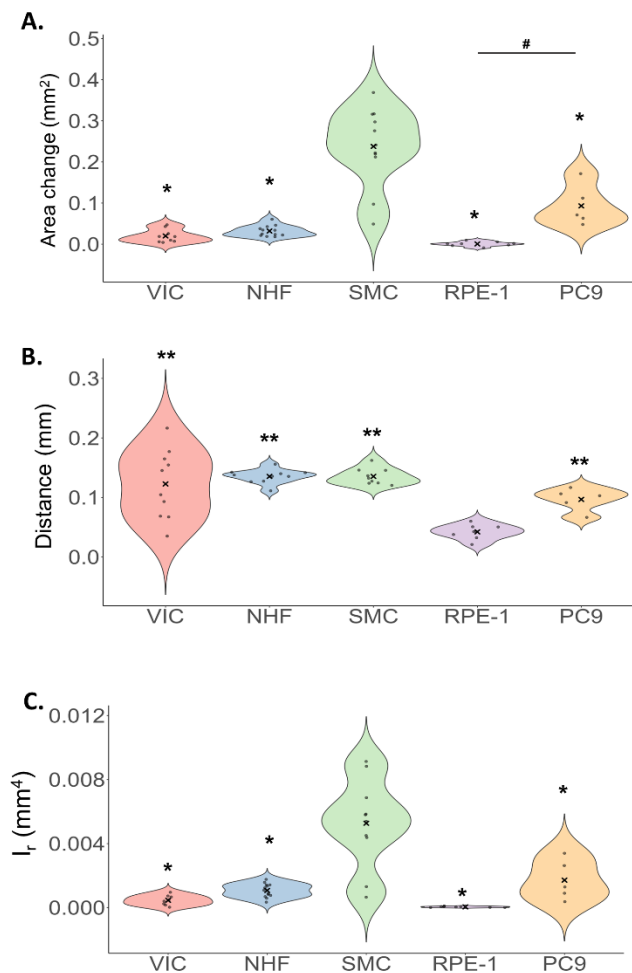
20

21

22

23

1



2

3 **Figure 5:** Quantitative metrics of invasion. Quantified area change (A), mean distance (B) and radial area
4 moment of inertia (I_r) (C) for VIC, NHF, SMC, PC9 and RPE-1 cells. Biological replicates are VIC=3,
5 NHF & SMC=2, and RPE-1 & PC9=1. Number of spheroids are indicated by dots on each plot and are:
6 VIC n=9, 10, 8 (A-C respectively), NHF n=12, 10, 13 (A-C respectively), SMC n=11, 9, 10 (A-C
7 respectively), RPE n=8 (all), PC9 n=5 (all). “x” indicates the mean value. Significance at $p < 0.05$
8 determined by one-way ANOVA with Tukey’s HSD post hoc test (exact p-values provided in
9 Supplementary Table 1). * and ** indicate significant difference to SMC (A) and (C) and RPE-1 (B)
10 respectively while # indicates significant difference between the specified groups (A).

11

12

1 **DISCUSSION**

2 In this work, we develop an *in vitro* imaging and analysis method to objectively assess the extent of cell
3 invasion from multicellular spheroids into a surrounding 3D hydrogel. Individual spheroids are imaged at
4 initial and final time points allowing for accurate determination of cell invasion over the culture period
5 and overcoming limitations of methods that only analyze the final state of invasion [34,38,41]. The
6 projected distribution of nuclear pixels past the Day 0 boundary is automatically identified to calculate
7 common invasion metrics, e.g., the increase in area and mean distance from the boundary, as well as the
8 area moment of inertia, our new integrative metric which quantifies how the pixels of the nuclei of
9 invading cells are distributed in the image. These metrics are calculated with reference to the initial
10 boundary of the spheroid at Day 0 which is automatically segmented. We introduce coordinate
11 transformation to identify the directions and extent of most and least invasion for cases where the
12 invasion may not be radially symmetric due to directional mechanical or chemical signaling gradients.
13 We demonstrate the utility of our method using five different cell types of varying invasive potentials and
14 show that the metrics quantitatively capture the differences in invasiveness among the cell types.

15 By automatically segmenting the initial spheroid to generate the boundary of invasion, we lessen the
16 effect that spheroid size differences can have on the invasion metrics. While this approach is not an all-
17 encompassing solution to the challenge of generating consistently sized spheroids, as demonstrated by the
18 variability in our invasion metric results (Figure 5), it aids in reducing the effect of spheroid size on
19 invasion metrics as previously described [47]. This approach is especially useful for cell types that do not
20 reliably form uniform spheroids (Supplementary Fig. 6) [30,37,60,61]. A limitation of this method is that
21 it assumes that invasion occurs from cells located at the spheroid boundary, thus it does not account for
22 the additional distance traveled by cells invading from deeper within the spheroid. However, this method
23 provides a key advantage over the majority of invasion quantification methods that assume all spheroids
24 are the same size [30,38,41,43,49]. Automated boundary segmentation makes spheroid invasion analysis

1 more flexible for non-uniform spheroid sizes and shapes and, by extension, makes it easier to quantify
2 spheroids of various cell types.

3 To our knowledge, we are the first to introduce a pixel-based method for invasion analysis. Using
4 pixels is less subjective than segmenting cells because it can be difficult to automatically distinguish
5 individual cells when they are clustered (Supplementary Fig. 7), and manual tracing of cell boundaries is
6 user-dependent and time consuming and cannot be completed if the cell boundaries are not evident
7 [8,30,37-43,62]. Automated spheroid invasion quantification methods such as TASI segment the spheroid
8 mass as one object and, as a result, are limited to assessing the distance of invasion from the spheroid
9 centroid or core boundary to the edge of a dense invasion front [47,48]. This limitation is also present in
10 machine learning approaches [63] as well as in methods that quantify morphological features for
11 spheroids not embedded in ECM, such as AnaSP and INSIDIA [62,64]. Our method has the key
12 advantage of accounting for all pixels past the boundary—a distinction especially important for cell types
13 (such as primary cells) which separate into individual clumps and do not form a dense collective invasion
14 front, as we have demonstrated in Figure 3 and 5.

15 To determine the sensitivity of our pixel-based approach to thresholding, we analyzed the dissociated
16 single nuclei invading from a representative spheroid at low, medium and high global threshold values
17 and compared the results to a standard object-based method (Supplementary Fig. 8). As the threshold is
18 decreased, an increasing number of pixels surpass the threshold value leading to larger area, distance and
19 moment values for both the pixel-based and object-based methods at comparable degrees. We expected
20 that the number of single nuclei identified in the object-based method would be less sensitive to threshold
21 than the pixel-based metrics because changing the threshold value would simply change the sizes of
22 binarized nuclei. However, we were surprised to find a non-monotonic relationship between the number
23 of single nuclei and the threshold. The number of nuclei increased when the threshold was decreased from
24 the high to medium values as expected, but the number of nuclei decreased from the medium and low
25 threshold values due to nuclei either coalescing into the spheroid bulk or merging together into a single

1 object too large to meet the size criteria for a single nucleus. Therefore, our pixel-based approach is not
2 only comparable to an object-based approach for calculating invasion metrics but also potentially
3 advantageous as it does not strictly report the “number” of cells or nuclei which, as we have
4 demonstrated, is highly sensitive to thresholding.

5 Maximum projection z-stack images of fluorescently stained nuclei were utilized since the nuclei are
6 high contrast and easy to binarize and can be easily stained for live imaging using inexpensive and readily
7 available stains, (e.g., Hoechst) and are common for 3D spheroid invasion analysis [30,41,44,48,65]. If
8 analysis of 3D invasion along the z-direction is needed, these methods can potentially be applied to
9 individual z-stack images [66]. Further, quantifying cell nuclei rather than the cell body results in more
10 accurate invasion area measurements because the cell nucleus, unlike the cell body, commonly resists
11 large changes in shape during cell migration and invasion [53] due to being 5-10 times stiffer than the
12 surrounding cytoskeleton [54]. This effect of cell shape on perceived cell size in 2D images is an issue
13 overlooked by studies that assume invading cells are all the same size [8,30,34,37,43,44,49]. Thus,
14 utilizing individual pixels of fluorescently stained nuclei is a powerful approach to quantifying spheroid
15 cell invasion.

16 We introduce the application of the classical area moment of inertia parameter, which reflects
17 how the points of an area are distributed with regard to an arbitrary axis, and apply it towards spheroid
18 invasion as an integrative “invasiveness” metric encompassing both the projected distance and area of
19 invasion. Thus, the area moment of inertia is a more informative metric than the area change or the mean
20 distance alone. While the area change metric is useful for representing the change in cell number over the
21 culture period [30,37,38,43,44], it may be skewed by variations in cell proliferation rates among cell
22 types. The mean distance does not have this limitation, but it does not provide insight into the cell number
23 [41]. Liu *et al.* use a similar metric combining cell area and distance of invasion (not squared as for the
24 area moment of inertia) [30]; however, their method requires manual image tracing of cells from a
25 uniform spherical bead whereas our metric is implemented more automatically and can be applied to

1 common, arbitrarily shaped spheroids. Using specific cases, we show that NHF and SMCs from
2 individual spheroids can have nearly identical invasiveness as measured by radial moment ($\sim 1.3 \times 10^{-3} \text{ mm}^4$)
3 yet substantially different area change and distance values (c.f., panels A and B in Fig. 3). Further, the
4 invasion of VICs can look qualitatively similar to that of NHF and have a similar area of invasion, yet
5 the radial moment is almost 30% smaller (c.f., panels A and 3 in Fig. 3). These results highlight the
6 limitations of the area change and distance metrics when used alone and demonstrate the importance of
7 the area moment of inertia metric which incorporates both area and distance to quantify cell invasion.

8 Quantifying invasion directionality for cell populations is important for determining the effects of
9 spatial gradients of chemical and mechanical factors. Most previous studies either track single cell
10 directional migration [8,38,39,46,67] or quantify invasion of a population of cells along one direction
11 [46,47]. We directly calculate the extent of invasion along x- and y-image axes using the area moment of
12 inertia (I_x and I_y) as well as estimate it using the mean distances in the x- and y-directions. For simpler
13 comparison, the extent of anisotropic invasion between cell types can be calculated by the fold change of
14 the directional moments and distances. Ibrahim *et al.* similarly calculate the mean distance in the
15 maximum invasion direction (by fitting it to an ellipse) [47]; however, their approach limits analysis to
16 only the contiguous portion of the spheroid and omits the isolated cells whereas our approach includes all
17 invaded cells. For greater generalizability, we also introduce the use of coordinate transformation to
18 account for cases when invasion does not occur strictly along the axes of the image. We showed that
19 calculating the mean distances and directional moments along the axes of maximum and minimum
20 invasion using PCA is a straight-forward way to characterize the extent of directionality of invasion. As a
21 demonstration, we applied the method to a spheroid cultured near a stiff silicone post which increases cell
22 invasion along its direction via contact guidance and found the invasion (as measured by area moment of
23 inertia) to be 2.2-fold higher in the direction of the post. This method can be used to assess the directional
24 invasion response to guidance cues applied in any direction (e.g., mechanical constraints and chemical
25 gradients); to our knowledge, we are the first to apply PCA to cell invasion analysis.

1 To expand user accessibility to our computer program, we have published an open-source graphical
2 user interface for researchers without training in computer programming. In addition, the source code is
3 also published in both Python (which is open-source) and MATLAB to allow for custom adaptation as
4 desired and to cater to the researcher's programming language preference. Taken together, these options
5 broaden the ease of use of this spheroid invasion quantification method to biomedical researchers with a
6 broad array of backgrounds.

7

8 **CONCLUSIONS**

9 Here we develop a high-throughput objective quantification method of cell invasion from multicellular
10 spheroids into a 3D extracellular matrix and demonstrate its utility with different metrics of invasion
11 applied to cell types of various invasive potentials. This pixel-based method can be applied to a variety of
12 spheroid invasion studies, such as exploring the roles of ECM components and guidance cues (e.g.,
13 chemokines and dynamic stretch) in cell invasion. The use of a nuclear stain minimizes the effect of cell
14 size variations, while live-staining the Day 0 spheroid allows for objective spheroid segmentation.
15 Calculating the distances of all pixels past the Day 0 boundary, which is unique to each spheroid,
16 minimizes the effects of spheroid size and shape on the calculated metrics of invasion. Thus, this
17 automated custom image analysis tool is complementary to traditional segmentation methods and is a
18 considerable addition to the field. We also introduce the area moment of inertia as an integrative metric of
19 cell invasion. The program also utilizes coordinate transformation to allow researchers to assess invasion
20 directionality in response to a guidance cue. This innovative approach to 3D cell invasion analysis has the
21 potential to advance research in fields including wound healing, cancer metastasis, and the repopulation
22 of decellularized tissue engineered scaffolds.

23

24

1 **DATA AVAILABILITY**

- 2 The datasets used and/or analyzed during the current study are available from the corresponding author on
- 3 reasonable request and are also available at the Harvard Dataverse using the following link:
- 4 <<https://doi.org/10.7910/DVN/VQH0BK> >

1 REFERENCES

- 2 1 Butcher, J. T. & Markwald, R. R. Valvulogenesis: the moving target. *Philos Trans R Soc Lond B*
3 *Biol Sci* **362**, 1489-1503, doi:10.1098/rstb.2007.2130 (2007).
- 4 2 Ahuja, N., Ostwald, P., Bark, D. & Garrity, D. Biomechanical Cues Direct Valvulogenesis. *J*
5 *Cardiovasc Dev Dis* **7**, doi:10.3390/jcdd7020018 (2020).
- 6 3 Elsdale, T. & Bard, J. Collagen substrata for studies on cell behavior. *J Cell Biol* **54**, 626-637,
7 doi:10.1083/jcb.54.3.626 (1972).
- 8 4 Singer, A. J. & Clark, R. A. Cutaneous wound healing. *N Engl J Med* **341**, 738-746,
9 doi:10.1056/nejm199909023411006 (1999).
- 10 5 Grinnell, F., Rocha, L. B., Iucu, C., Rhee, S. & Jiang, H. Nested collagen matrices: a new model
11 to study migration of human fibroblast populations in three dimensions. *Exp Cell Res* **312**, 86-94,
12 doi:10.1016/j.yexcr.2005.10.001 (2006).
- 13 6 Guillamat-Prats, R. The Role of MSC in Wound Healing, Scarring and Regeneration. *Cells* **10**,
14 doi:10.3390/cells10071729 (2021).
- 15 7 Hayward, M.-K., Muncie, J. M. & Weaver, V. M. Tissue mechanics in stem cell fate,
16 development, and cancer. *Developmental cell* **56**, 1833-1847 (2021).
- 17 8 Heussner, R. K., Zhang, H., Qian, G., Baker, M. J. & Provenzano, P. P. Differential contractility
18 regulates cancer stem cell migration. *Biophys J* **122**, 1198-1210, doi:10.1016/j.bpj.2023.02.008
19 (2023).
- 20 9 SenGupta, S., Parent, C. A. & Bear, J. E. The principles of directed cell migration. *Nat Rev Mol*
21 *Cell Biol* **22**, 529-547, doi:10.1038/s41580-021-00366-6 (2021).
- 22 10 VeDepo, M. C., Detamore, M. S., Hopkins, R. A. & Converse, G. L. Recellularization of
23 decellularized heart valves: Progress toward the tissue-engineered heart valve. *J Tissue Eng* **8**,
24 2041731417726327, doi:10.1177/2041731417726327 (2017).
- 25 11 Syedain, Z. H., Maciver, R. & Tranquillo, R. T. Vascular grafts and valves that animate, made
26 from decellularized biologically-engineered tissue tubes. *J Cardiovasc Surg (Torino)* **61**, 577-
27 585, doi:10.23736/s0021-9509.20.11615-x (2020).
- 28 12 Syedain, Z. H. *et al.* Pediatric tri-tube valved conduits made from fibroblast-produced
29 extracellular matrix evaluated over 52 weeks in growing lambs. *Sci Transl Med* **13**,
30 doi:10.1126/scitranslmed.abb7225 (2021).
- 31 13 Bouten, C. V. C., Smits, A. & Baaijens, F. P. T. Can We Grow Valves Inside the Heart?
32 Perspective on Material-based In Situ Heart Valve Tissue Engineering. *Front Cardiovasc Med* **5**,
33 54, doi:10.3389/fcvm.2018.00054 (2018).
- 34 14 Shellard, A. & Mayor, R. All Roads Lead to Directional Cell Migration. *Trends Cell Biol* **30**,
35 852-868, doi:10.1016/j.tcb.2020.08.002 (2020).
- 36 15 Zonderland, J. & Moroni, L. Steering cell behavior through mechanobiology in 3D: A
37 regenerative medicine perspective. *Biomaterials* **268**, 120572 (2021).
- 38 16 Deng, B. *et al.* Biological role of matrix stiffness in tumor growth and treatment. *J Transl Med*
39 **20**, 540, doi:10.1186/s12967-022-03768-y (2022).
- 40 17 Roby, T., Olsen, S. & Nagatomi, J. Effect of sustained tension on bladder smooth muscle cells in
41 three-dimensional culture. *Ann Biomed Eng* **36**, 1744-1751, doi:10.1007/s10439-008-9545-5
42 (2008).
- 43 18 Tondon, A. & Kaunas, R. The direction of stretch-induced cell and stress fiber orientation
44 depends on collagen matrix stress. *PLoS One* **9**, e89592, doi:10.1371/journal.pone.0089592
45 (2014).
- 46 19 Throm Quinlan, A. M., Sierad, L. N., Capulli, A. K., Firstenberg, L. E. & Billiar, K. L.
47 Combining dynamic stretch and tunable stiffness to probe cell mechanobiology in vitro. *PLoS*
48 *One* **6**, e23272, doi:10.1371/journal.pone.0023272 (2011).

- 1 20 Quinlan, A. M. & Billiar, K. L. Investigating the role of substrate stiffness in the persistence of
2 valvular interstitial cell activation. *J Biomed Mater Res A* **100**, 2474-2482,
3 doi:10.1002/jbm.a.34162 (2012).
- 4 21 Cirka, H. *et al.* Active Traction Force Response to Long-Term Cyclic Stretch Is Dependent on
5 Cell Pre-stress. *Biophys J* **110**, 1845-1857, doi:10.1016/j.bpj.2016.02.036 (2016).
- 6 22 Jebeli, M. *et al.* Multicellular aligned bands disrupt global collective cell behavior. *Acta Biomater*
7 **163**, 117-130, doi:10.1016/j.actbio.2022.10.041 (2023).
- 8 23 Desai, L. P., Chapman, K. E. & Waters, C. M. Mechanical stretch decreases migration of alveolar
9 epithelial cells through mechanisms involving Rac1 and Tiam1. *Am J Physiol Lung Cell Mol*
10 *Physiol* **295**, L958-965, doi:10.1152/ajplung.90218.2008 (2008).
- 11 24 Boulter, E., Tissot, F. S., Dilly, J., Pisano, S. & Féral, C. C. Cyclic uniaxial mechanical stretching
12 of cells using a LEGO® parts-based mechanical stretcher system. *J Cell Sci* **133**,
13 doi:10.1242/jcs.234666 (2020).
- 14 25 Klingberg, F. *et al.* Prestress in the extracellular matrix sensitizes latent TGF-β1 for activation.
15 *The Journal of cell biology* **207**, 283-297, doi:10.1083/jcb.201402006 (2014).
- 16 26 Zhang, B. *et al.* Cyclic mechanical stretching promotes migration but inhibits invasion of rat bone
17 marrow stromal cells. *Stem Cell Research* **14**, 155-164,
18 doi:https://doi.org/10.1016/j.scr.2015.01.001 (2015).
- 19 27 Song, J. *et al.* Physiological cyclic stretch up-regulates angiotensin-converting enzyme 2
20 expression to reduce proliferation and migration of vascular smooth muscle cells. *Biosci Rep* **40**,
21 doi:10.1042/bsr20192012 (2020).
- 22 28 Balachandran, K., Sucusky, P., Jo, H. & Yoganathan, A. P. Elevated cyclic stretch alters matrix
23 remodeling in aortic valve cusps: implications for degenerative aortic valve disease. *American*
24 *Journal of Physiology-Heart and Circulatory Physiology* **296**, H756-H764 (2009).
- 25 29 Balachandran, K. *et al.* Cyclic strain induces dual-mode endothelial-mesenchymal transformation
26 of the cardiac valve. *Proceedings of the National Academy of Sciences* **108**, 19943-19948 (2011).
- 27 30 Liu, H., Lu, T., Kremers, G.-J., Seynhaeve, A. L. B. & ten Hagen, T. L. M. A microcarrier-based
28 spheroid 3D invasion assay to monitor dynamic cell movement in extracellular matrix. *Biological*
29 *Procedures Online* **22**, 3, doi:10.1186/s12575-019-0114-0 (2020).
- 30 31 Bakker, E. R. M. *et al.* Wnt5a promotes human colon cancer cell migration and invasion but does
31 not augment intestinal tumorigenesis in Apc 1638N mice. *Carcinogenesis* **34**, 2629-2638,
32 doi:10.1093/carcin/bgt215 (2013).
- 33 32 Janmaat, V. T. *et al.* HOXA9 mediates and marks premalignant compartment size expansion in
34 colonic adenomas. *Carcinogenesis* **40**, 1514-1524, doi:10.1093/carcin/bgz038 (2019).
- 35 33 Dietrich, F. & Lelkes, P. I. Fine-tuning of a three-dimensional microcarrier-based angiogenesis
36 assay for the analysis of endothelial-mesenchymal cell co-cultures in fibrin and collagen gels.
37 *Angiogenesis* **9**, 111-125 (2006).
- 38 34 Arevalos, C. A. *et al.* Valve Interstitial Cells Act in a Pericyte Manner Promoting Angiogenesis
39 and Invasion by Valve Endothelial Cells. *Ann Biomed Eng* **44**, 2707-2723, doi:10.1007/s10439-
40 016-1567-9 (2016).
- 41 35 Kniazeva, E. & Putnam, A. J. Endothelial cell traction and ECM density influence both capillary
42 morphogenesis and maintenance in 3-D. *American Journal of Physiology-Cell Physiology* **297**,
43 C179-C187 (2009).
- 44 36 Juliar, B. A., Keating, M. T., Kong, Y. P., Botvinick, E. L. & Putnam, A. J. Sprouting
45 angiogenesis induces significant mechanical heterogeneities and ECM stiffening across length
46 scales in fibrin hydrogels. *Biomaterials* **162**, 99-108 (2018).
- 47 37 Cisneros Castillo, L. R., Oancea, A. D., Stüllein, C. & Régnier-Vigouroux, A. Evaluation of
48 Consistency in Spheroid Invasion Assays. *Sci Rep* **6**, 28375, doi:10.1038/srep28375 (2016).
- 49 38 Elosegui-Artola, A. *et al.* Matrix viscoelasticity controls spatiotemporal tissue organization.
50 *Nature Materials*, doi:10.1038/s41563-022-01400-4 (2022).

- 1 39 Ray, A., Slama, Z. M., Morford, R. K., Madden, S. A. & Provenzano, P. P. Enhanced Directional
2 Migration of Cancer Stem Cells in 3D Aligned Collagen Matrices. *Biophys J* **112**, 1023-1036,
3 doi:10.1016/j.bpj.2017.01.007 (2017).
- 4 40 Solbu, A. A. *et al.* Assessing cell migration in hydrogels: An overview of relevant materials and
5 methods. *Materials Today Bio* **18**, 100537, doi:https://doi.org/10.1016/j.mtbio.2022.100537
6 (2023).
- 7 41 Ducker, M., Millar, V., Ebner, D. & Szele, F. G. A Semi-automated and Scalable 3D Spheroid
8 Assay to Study Neuroblast Migration. *Stem Cell Reports* **15**, 789-802,
9 doi:https://doi.org/10.1016/j.stemcr.2020.07.012 (2020).
- 10 42 Dolega, M. *et al.* Mechanical behavior of multi-cellular spheroids under osmotic compression.
11 *Journal of the Mechanics and Physics of Solids* **147**, 104205 (2021).
- 12 43 Nandi, S. & Brown, A. C. Characterizing Cell Migration Within Three-dimensional In Vitro
13 Wound Environments. *J Vis Exp*, doi:10.3791/56099 (2017).
- 14 44 Baskaran, J. P. *et al.* Cell shape, and not 2D migration, predicts extracellular matrix-driven 3D
15 cell invasion in breast cancer. *APL Bioeng* **4**, 026105, doi:10.1063/1.5143779 (2020).
- 16 45 Schneckenburger, H. & Richter, V. in *Photonics*. 275 (MDPI).
- 17 46 Rouillard, A. D. & Holmes, J. W. Mechanical boundary conditions bias fibroblast invasion in a
18 collagen-fibrin wound model. *Biophys J* **106**, 932-943, doi:10.1016/j.bpj.2013.12.002 (2014).
- 19 47 Ibrahim, H. *et al.* A Biomimetic high throughput model of cancer cell spheroid dissemination
20 onto aligned fibrillar collagen. *SLAS technology* **27**, 267-275 (2022).
- 21 48 Hou, Y., Konen, J., Brat, D. J., Marcus, A. I. & Cooper, L. A. TASI: A software tool for spatial-
22 temporal quantification of tumor spheroid dynamics. *Scientific reports* **8**, 7248 (2018).
- 23 49 Mina, S. G., Huang, P., Murray, B. T. & Mahler, G. J. The role of shear stress and altered tissue
24 properties on endothelial to mesenchymal transformation and tumor-endothelial cell interaction.
25 *Biomicrofluidics* **11**, 044104, doi:10.1063/1.4991738 (2017).
- 26 50 Menon, S. & Beningo, K. A. Cancer cell invasion is enhanced by applied mechanical stimulation.
27 *PLoS One* **6**, e17277, doi:10.1371/journal.pone.0017277 (2011).
- 28 51 O'Leary, R. & Wood, E. J. A novel in vitro dermal wound-healing model incorporating a
29 response to mechanical wounding and repopulation of a fibrin provisional matrix. *In Vitro Cell*
30 *Dev Biol Anim* **39**, 204-207, doi:10.1290/1543-706x(2003)039<0204:Anivdw>2.0.Co;2 (2003).
- 31 52 Petroll, W. M., Lakshman, N. & Ma, L. Experimental models for investigating intra-stromal
32 migration of corneal keratocytes, fibroblasts and myofibroblasts. *J Funct Biomater* **3**, 183-198,
33 doi:10.3390/jfb3010183 (2012).
- 34 53 McGregor, A. L., Hsia, C.-R. & Lammerding, J. Squish and squeeze—the nucleus as a physical
35 barrier during migration in confined environments. *Current Opinion in Cell Biology* **40**, 32-40,
36 doi:https://doi.org/10.1016/j.ceb.2016.01.011 (2016).
- 37 54 Friedl, P., Wolf, K. & Lammerding, J. Nuclear mechanics during cell migration. *Curr Opin Cell*
38 *Biol* **23**, 55-64, doi:10.1016/j.ceb.2010.10.015 (2011).
- 39 55 Rassias, D. J. & Weathers, P. J. Dried leaf *Artemisia annua* efficacy against non-small cell lung
40 cancer. *Phytomedicine* **52**, 247-253, doi:10.1016/j.phymed.2018.09.167 (2019).
- 41 56 Coutts, C. W. *et al.* The Role of Apoptosis and Oxidative Stress in a Cell Spheroid Model of
42 Calcific Aortic Valve Disease. *Cells* **13**, 45 (2024).
- 43 57 Miron-Mendoza, M., Seemann, J. & Grinnell, F. The differential regulation of cell motile activity
44 through matrix stiffness and porosity in three dimensional collagen matrices. *Biomaterials* **31**,
45 6425-6435, doi:10.1016/j.biomaterials.2010.04.064 (2010).
- 46 58 Matsumoto, T. *et al.* Three-dimensional cell and tissue patterning in a strained fibrin gel system.
47 *PloS one* **2**, e1211-e1211, doi:10.1371/journal.pone.0001211 (2007).
- 48 59 Pelham, R. J., Jr. & Wang, Y. I. Cell locomotion and focal adhesions are regulated by substrate
49 flexibility. *Proceedings of the National Academy of Sciences of the United States of America* **94**,
50 13661-13665, doi:10.1073/pnas.94.25.13661 (1997).

- 1 60 Vinci, M. *et al.* Advances in establishment and analysis of three-dimensional tumor spheroid-
2 based functional assays for target validation and drug evaluation. *BMC biology* **10**, 1-21 (2012).
- 3 61 Dolznig, H. *et al.* Modeling colon adenocarcinomas in vitro: A 3D co-culture system induces
4 cancer-relevant pathways upon tumor cell and stromal fibroblast interaction. *The American*
5 *journal of pathology* **179**, 487-501 (2011).
- 6 62 Piccinini, F. AnaSP: A software suite for automatic image analysis of multicellular spheroids.
7 *Computer Methods and Programs in Biomedicine* **119**, 43-52,
8 doi:<https://doi.org/10.1016/j.cmpb.2015.02.006> (2015).
- 9 63 Ngo, T. K. N. *et al.* A deep learning-based pipeline for analyzing the influences of interfacial
10 mechanochemical microenvironments on spheroid invasion using differential interference
11 contrast microscopic images. *Materials Today Bio* **23**, 100820 (2023).
- 12 64 Perini, G. *et al.* INSIDIA 2.0 high-throughput analysis of 3D cancer models: multiparametric
13 quantification of graphene quantum dots photothermal therapy for glioblastoma and pancreatic
14 cancer. *International Journal of Molecular Sciences* **23**, 3217 (2022).
- 15 65 Huang, Y. L. *et al.* Tumor spheroids under perfusion within a 3D microfluidic platform reveal
16 critical roles of cell-cell adhesion in tumor invasion. *Scientific Reports* **10**, 9648,
17 doi:[10.1038/s41598-020-66528-2](https://doi.org/10.1038/s41598-020-66528-2) (2020).
- 18 66 Weiss, F. *et al.* 3D spheroid culture to examine adaptive therapy response in invading tumor cells.
19 *In Vitro Model* **1**, 463-471, doi:[10.1007/s44164-022-00040-x](https://doi.org/10.1007/s44164-022-00040-x) (2022).
- 20 67 Pang, Y., Wang, X., Lee, D. & Greisler, H. P. Dynamic quantitative visualization of single cell
21 alignment and migration and matrix remodeling in 3-D collagen hydrogels under mechanical
22 force. *Biomaterials* **32**, 3776-3783, doi:[10.1016/j.biomaterials.2011.02.003](https://doi.org/10.1016/j.biomaterials.2011.02.003) (2011).

23

1 **ACKNOWLEDGEMENTS**

2 The assistance provided by Jamie Baines in conducting experiments is gratefully acknowledged.

3 This work was supported by the National Science Foundation (NSF) [CMMI 1761432], the National

4 Institutes of Health (NIH) [1R15HL167235-01] and the American Heart Association (AHA)

5 [20AIREA35120448]. The funders had no role in study design, data collection and analysis, decision to

6 publish, or manuscript preparation.

7

8 **AUTHOR INFORMATION**

9 *Affiliations*

10 **Department of Biomedical Engineering, Worcester Polytechnic Institute, Worcester, MA, USA**
11 **01605.**

12 Rozanne W. Mungai, Grace E. Jolin, Kevin W. Piskorowski and Kristen L. Billiar

13 **No affiliations. Independent researcher, Worcester, MA, USA 01605.**

14 Roger J. Hartman II

15

16 *Contributions*

17 K.L.B. and R.W.M. conceived the experiment which was performed by R.W.M., G.E.J., and K.W.P..

18 Results analysis was performed by R.W.M. who also quantified the data using MATLAB. R.J.H.II

19 translated the quantification methods to Python and designed the GUI. R.W.M. wrote the manuscript draft

20 which was edited by K.L.B. All authors approved the final version of the manuscript.

21

22 **ETHICS DECLARATIONS**

23 *Competing interests*

1 The authors declare no competing financial interests.

1 **FIGURE LEGENDS**

2 **Figure 1: Z-stack image processing and quantification.** Images were processed to create maximum z-
3 projection images from each z-stack as demonstrated by a representative Day 2 image (A). The Day 0
4 boundary was segmented (B) and the pixels of the Day 2 image located past the boundary were identified
5 (C). The distances and angles of the pixels outside of the boundary were calculated with reference to the
6 spheroid boundary and center. For clarity, only a portion of the distance lines are shown (D). Scale bar:
7 200 μ m. Panel A: Representative spheroid is imaged at 20X magnification and off-set to highlight
8 invading cells. Panels B-D: 10X magnification.

9
10 **Figure 2: Invasion of cells from spheroids into collagen hydrogels.** Representative images of invasion
11 on Day 0 compared to Day 2, VIC (A), NHF (B), SMC (C), RPE-1 (D) and PC9 (E). Binarized maximum
12 projection images of cell nuclei stained with Hoechst fluorescent dye at 10X magnification. Scale bar:
13 200 μ m

14
15 **Figure 3: Visualization of variation of invasion behavior across cell types.** Polar plots demonstrate
16 invasion behavior of individual spheroids at Day 2. The distance (μ m) versus angle is plotted for each
17 pixel past the Day 0 spheroid boundary for VIC (A), NHF (B), SMC (C), RPE-1 (D) and PC9 (E). The
18 boundary is represented as the plot center (0,0). Invasion metrics for representative spheroids, area
19 change, ΔA , mean distance, \bar{D} , radial moment, I_r , as defined in the text, are provided below each plot.

20
21 **Figure 4: Quantification program also assesses invasion directionality.** Directional invasion was
22 demonstrated by imaging a collagen gel-embedded VIC spheroid growing near a structural post (indicated
23 by arrow) of the culture well for four days. Phase, Hoechst-stained and binarized spheroid images on Day

1 2 (no post control) and Day 4 (spheroid with post). Scale bar: 200 μm (A-C). PCA of quantified data
2 plotted as a polar plot centered at the mean. Principal angles are indicated (blue line: maximum invasion
3 at 125° and -12°; black line: minimum invasion). Polar plot depicts the distance from the boundary (mm)
4 versus angle for each pixel. Mean distances and directional moments along the principal angles were
5 calculated to quantify invasion directionality and are provided below the polar plot (D).

6

7 **Figure 5: Quantitative metrics of invasion.** Quantified area change (A), mean distance (B) and radial
8 area moment of inertia (I_r) (C) for VIC, NHF, SMC, PC9 and RPE-1 cells. Biological replicates are
9 VIC=3, NHF & SMC=2, and RPE-1 & PC9=1. Number of spheroids are indicated by dots on each plot
10 and are: VIC n=9, 10, 8 (A-C respectively), NHF n=12, 10, 13 (A-C respectively), SMC n=11, 9, 10 (A-C
11 respectively), RPE n=8 (all), PC9 n=5 (all). “x” indicates the mean value. Significance at $p < 0.05$
12 determined by one-way ANOVA with Tukey’s HSD post hoc test (exact p-values provided in
13 Supplementary Table 1). * and ** indicate significant difference to SMC (A) and (C) and RPE-1 (B)
14 respectively while # indicates significant difference between the specified groups (A).

15